The Dynamic Wavelet Fingerprint Process (DWFP): Revealing hidden information in noisy signals

Many measurements acquired from physical systems are one-dimensional time domain signals, commonly representing amplitude as a function of time. As signals become more complicated or noisy it becomes difficult to extract useful information from the signal directly. Features that were previously used to differentiate signals no longer do so reliably. Here we discuss how we can find new, useful features that describe our signal by creating representations of the original one-dimensional time domain signal in alternative domains. These transformations reveal useful features hidden inside the original signal at the expense of a more abstract connection to the original signal.

In particular, we introduce the Dynamic Wavelet Fingerprint Process (DWFP), which has proven adept at revealing hidden information in extremely noisy real-world signals. The basic idea of this technique is to generate an intuitive two-dimensional pattern in the time-scale domain from which significant features can be extracted either directly or by using statistical pattern recognition algorithms. These features are then used to identify specific points of interest for detection and classification. Successful prior applications include the detection and classification of material flaws using ultrasound [1, 2, 3], early detection of periodontal disease [4, 5], identification of wiring flaws using time domain reflectometry [6], prediction of roof fall events in underground mines [7], and automated vehicle classification using an acoustic echolocation sensor [8].

1 Time-frequency analysis of signals

1.1 Existing methods

The most common transformation of a one-dimensional signal uses the Fourier transform to convert a real signal $f(t)$ to the frequency domain

$$\mathfrak{F}(\omega) = \frac{1}{\sqrt{2\pi}} \int_{-\infty}^{\infty} f(t)\, e^{-i\omega t} dt, \tag{1}$$

with symmetric inverse transform

$$f(t) = \frac{1}{\sqrt{2\pi}} \int_{-\infty}^{\infty} \mathfrak{F}(\omega)\, e^{i\omega t} d\omega. \tag{2}$$

This essentially decomposes any periodic signal into a sum of sines and cosines, highlighted by looking at the Fourier series

$$f(t) = \frac{a_0}{2} + \sum_{n=1}^{\infty} a_n \cos(nt) + b_n \sin(nt), \tag{3}$$

where the a_n and b_n are the Fourier coefficients. By finding the values of these coefficients that best describe the original signal, we are describing the signal in terms of some new basis functions, here, sines and cosines[1].

In practice, calculation of the Fourier transform is accomplished using a discrete Fourier transform, for which any number of stable, fast algorithms exist. Accurate reconstruction is guaranteed as long as the Nyquist-Shannon sampling theorem is respected whereby the sampling rate f_s must be at least twice the maximum frequency content present in the signal.

While the Fourier transform allows us to examine the frequency content of a signal over long time durations, often times the signal content gets obscured by transient events such as high energy bursts. One simple solution to this problem is to look at the Fourier transform over a series of short windows along the length of the signal. This is called the Short-Time Fourier Transform (STFT), implemented as

$$\textbf{STFT}\left\{f(t)\right\}(\tau,\omega) \equiv \mathfrak{F}(\tau,\omega) = \frac{1}{\sqrt{2\pi}} \int_{-\infty}^{\infty} f(t)\, \bar{w}(t-\tau)\, e^{-i\omega t} dt, \tag{4}$$

where $\bar{w}(t-\tau)$ is a windowing function that is nonzero for only a short time (typically a Hann window, described in the discrete domain by $\bar{w}(n) = \sin^2\left(\frac{\pi n}{N-1}\right)$) [9, 10].

[1] The relation to the complex exponential given in the Fourier transform comes from Euler's formula, $e^{2\pi i\theta} = \cos 2\pi\theta + i \sin 2\pi\theta$.

This transformation from the one-dimensional time domain to a joint time-frequency domain creates a two-dimensional representation of the signal, giving us more information about our signal. The spectrogram (or waterfall plot), displaying the STFT squared magnitude ($|\mathfrak{F}(\tau,\omega)|^2$) as a color-mapped image with frequency on the vertical axis and time on the horizontal axis, shows the evolution of the frequency spectrum with time.

However, the uncertainty principle known as the Gabor limit reveals a more serious limitation of the STFT. This statement,

$$\Delta t\ \Delta\omega \geq \frac{1}{2}, \tag{5}$$

states that a function cannot be both time and band limited, or in other words, it is impossible to simultaneously localize a function in both the time and the frequency domains. This leads to resolution issues for the STFT – a short window will provide precise temporal resolution and poor frequency resolution, while a wide window has the exact opposite effect [11].

A number of alternative time-frequency representations have been created in an attempt to improve the resolution issues with the STFT[2]. These include the time-frequency formulation of the Wigner-Ville distribution

$$W(\tau,\omega) = \int_{-\infty}^{\infty} f\left(\tau + \frac{t}{2}\right) f^*\left(\tau - \frac{t}{2}\right)\ e^{-i\omega t} dt \tag{6}$$

where $f^*(t)$ is the complex conjugate of $f(t)$. This is a specialized form of the power spectral density (PSD) function

$$S(\omega) = \int_{-\infty}^{\infty} f(t) f^*(t-\tau)\ e^{-i\omega t} dt, \tag{7}$$

which can be interpreted as the Fourier transform of the autocorrelation of the original signal $f(t)$. Because this is not a linear transform, cross terms occur when the input signal is not monochromatic [12]. Combining Wigner-Ville with Gabor's eponymous improvement to the STFT,

$$G(\tau,\omega) = \int_{-\infty}^{\infty} e^{-\pi(t-\tau)^2}\ e^{-i\omega t}\ f(t)\ dt, \tag{8}$$

which is basically the STFT with a Gaussian window function, allows us to mitigate the effects of the cross terms and improve the resolution of the time-frequency representation [13]. One possible representation of this Gabor-Wigner transform is

$$D(\tau,\omega) = G(\tau,\omega) \times W(\tau,\omega). \tag{9}$$

1.2 Wavelets

The overarching issue with any of the time-frequency methods previously discussed is that the basis of the Fourier transform is chosen with the assumption that the signals to be analyzed are periodic or infinite in time, whereas most real-world signals are not periodic. One good example comes from attempting to approximate a finite signal with sharp discontinuities (such as a square wave) using a linear combination of sinusoids, which creates large oscillations near the discontinuities. Known as the Gibbs phenomenon, this overshoot increases with frequency (as more sums are added to the Fourier series) but eventually approaches a finite limit.

Instead we can use a basis of finite signals, called wavelets, to better approximate real-world signals. The wavelet transform is written as

$$\mathfrak{W}(\tau,s) = \frac{1}{\sqrt{s}} \int_{-\infty}^{\infty} f(t)\ \psi\left(\frac{t-\tau}{s}\right) dt. \tag{10}$$

A comparison to the STFT (Equation 4) shows that this transform decomposes the signal not into linear combinations of sines and cosines, but into linear combinations of wavelet functions $\psi(\tau,s)$. We can relate this to the Fourier decomposition (3) by defining the wavelet coefficients

$$c_{jk} = \mathfrak{W}\left(k2^{-j}, 2^{-j}\right). \tag{11}$$

[2]Interestingly, most were created in the mid-20$^{\text{th}}$ century alongside the development of quantum mechanics due to the similar mathematics in the position-momentum and time-frequency domains.

Here, $\tau = k2^{-j}$ and is referred to as the dyadic position and $s = 2^{-j}$ and is called the dyadic dilation. Basically, we are decomposing our signal in terms of a wavelet that can move (position τ) and deform by stretching or shrinking (scale s). This transforms our original signal into a joint time-scale domain, rather than a frequency domain (Fourier transform) or joint time-frequency domain (STFT). Although the wavelet transform doesn't provide any direct frequency information, scale is related to the inverse of frequency, with low scale decompositions relating to high frequency and vice-versa. In addition to representing near-discontinuous signals better than the STFT, the dyadic (factor-of-two) decomposition of the wavelet transform allows an improvement in time resolution at high frequencies (Figure 1).

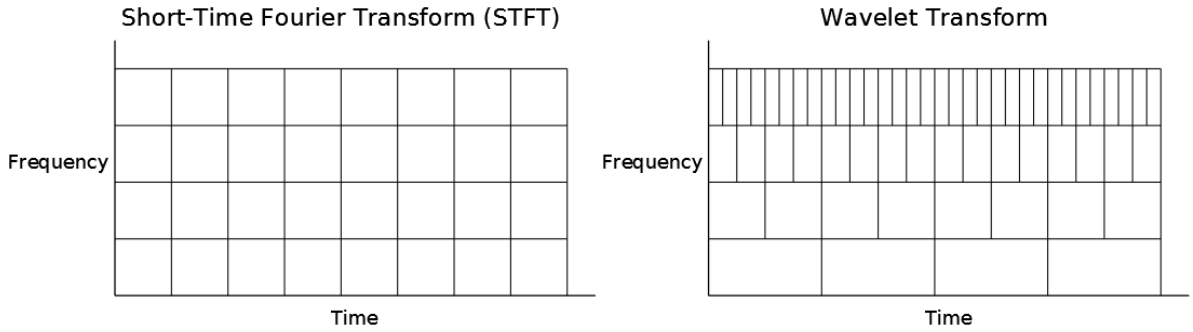

Figure 1: The STFT has similar time resolution at all frequencies, while the dyadic nature of the wavelet transform affords better time resolution at high frequencies (low scale values)

Wavelets are completely described in the time domain by the wavelet function (mother wavelet $\psi(t)$) and a scaling function (father wavelet $\phi(t)$). The scaling function is necessary because stretching the wavelet in the time domain reduces the bandwidth, requiring an infinite number of wavelets to accurately capture the entire spectrum. This is similar to Zeno's paradox, in which trying to get from point A to point B by crossing half the remaining distance each time is ultimately fruitless. The scaling function is an engineering solution to this problem, allowing us to get close enough for all practical purposes by covering the rest of the spectrum [14].

In general, any continuous signal can be represented by a linear combination of orthonormal basis functions (specifically, the basis functions must define a Hilbert space). Since as part of the decomposition we are allowed to scale and shift our original wavelet, we only need to ensure that the mother wavelet is continuously differentiable and compactly supported to fulfill this condition.

The Haar wavelet is the simplest example – a discontinuous step function with uniform scaling function. This is also the first (db1) of the Daubechies family of wavelets abbreviated dbN, with order N (which is the number of vanishing moments). Historically, these were the first compactly supported orthonormal set of wavelets, shortly followed by Daubechies' slightly modified and least asymmetric Symlet family. The Coiflet family, also exhibiting vanishing moments, were also created by Daubechies at the request of other researchers [15]. The Meyer wavelet has both its scaling and wavelet functions defined in the frequency domain, but is not technically a wavelet because its wavelet function is not compactly supported. However, $\psi \to 0$ as $x \to \infty$ fast enough that the pseudo-wavelet is infinitely differentiable. This allows the existence of good approximations for use in discrete wavelet transforms. Both the Mexican hat and Morlet wavelets are explicitly defined and have no scaling function. The Mexican hat wavelet is proportional to the second derivative function of the Gaussian probability density function, while the Morlet wavelet is defined as $\psi(x) = Ce^{-x^2}\cos(5x)$, with scaling constant C.

2 The Dynamic Wavelet Fingerprint (DWFP)

So far we have seen both the benefits and difficulties present in several different methods of time-frequency analysis. While alternative time-frequency transformations can improve the resolution limits of the STFT, they create their own problems such as the cross-term in the Wigner-Ville transform. Combinations of transforms can reduce these effects while still offering increased resolution, but this comes at the cost of computational complexity. Wavelets offer an alternative basis for decomposition that is more suited to finite real-world signals, but lacks a direct relationship to frequency.

One of the yet undiscussed issues with time-frequency representations of signals is the added complexity of the resultant time-frequency images. Just as displaying a one-dimensional signal requires a two-dimensional image, viewing a two-dimensional signal requires a three-dimensional visualization method. Common techniques include three-dimensional surface plots that can be rotated on a computer screen or colormapped two-dimensional images where the value at each point is mapped to a color.

While these visualizations work well for human interpretation of the images, computers have a difficult time distinguishing between those parts of the image we care about and those that are just background. This difficulty with image segmentation is especially true for noisy signals. The human visual system is evolutionarily adapted to be quite good at this (in previous times, detecting a lion hiding in the tall grass was a matter of life or death), but computers lack such an advantage.

That being said, computers may have an advantage over humans when it comes to selective attention, as famously illustrated by [16]. In this example, viewers are shown a video in which a group of people are running around with a basketball and told to count the total number of times the ball is passed. Halfway through the video a man in a gorilla suit walks across the frame, directly through the group, and yet is invariably unnoticed by the viewer whose attention is focused elsewhere.

There is also the limitation of suitable algorithms – current automated image segmentation methods work well for scenes where a single object is moving in a predictable path across a mostly stationary background [17, 18, 19].

Our DWFP technique mitigates these problems of segmentation and attention by transforming a one-dimensional time domain waveform to a two-dimensional, pre-segmented time-scale image that can be analyzed using existing image processing techniques.

2.1 Feature creation

To suppress noise and high-frequency interference that may cause distortion of the DWFP fingerprint image created later, the original one-dimensional signal is first filtered using a discrete wavelet transform [20, 21]. The signal is decomposed into stationary wavelet coefficients $W_S(\tau, s)$ at scale s and time τ and then pruned by setting the wavelet coefficients at small scales (high frequencies) to zero

$$W_S(\tau, s) = 0 \text{ for } s = 1, \ldots, 5. \tag{12}$$

A Tukey window can also be applied to the filtered signal at this point to smooth behavior at the edges.

The filtered signal is then subjected to the processing illustrated in Figure 2. Wavelet coefficients are created using a continuous wavelet transform with given wavelet $\psi(x)$. Different choices for the mother wavelet will produce different images, some of which will better highlight features of interest in the signals under study than others. The wavelet coefficients, which form a three-dimensional surface, are then normalized into the range [-1, 1] and bi-directionally projected onto the time-scale plane. This generates a ternary image (often resembling a set of fingerprints), where positive coefficients are mapped to a white value, negative coefficients are mapped to a grey value, and the background remains black. This abstract two-dimension representation, with time on the horizontal axis and wavelet scale on the vertical axis, allows patterns in the data to be recognized even when none are evident in the one-dimensional waveforms.

2.2 Feature extraction

A number of features can be extracted from this fingerprint image using standard image processing libraries [23]. The resemblance of our images to fingerprints, for which a large image recognition literature already exists, can be exploited in this process [24, 25]. Some of the features we extract are by definition continuous, for example, a simple count of the number of ridges at each time point. However, many of the features that we want to extract from the image are tied to a particular individual fingerprint, requiring us to first identify and consecutively label the individual fingerprints. We use a measure of nearly connectedness, in which pixels of the same value within a set distance of each other are considered connected, to label each individual fingerprint.

These extracted features are then linearly interpolated to form parameter waveforms and facilitate a direct comparison to the original time domain signal. Approximately 25 one-dimensional parameter waveforms are normally created for each individual measurement. Some of the extracted features are explained in more detail in Table 1.

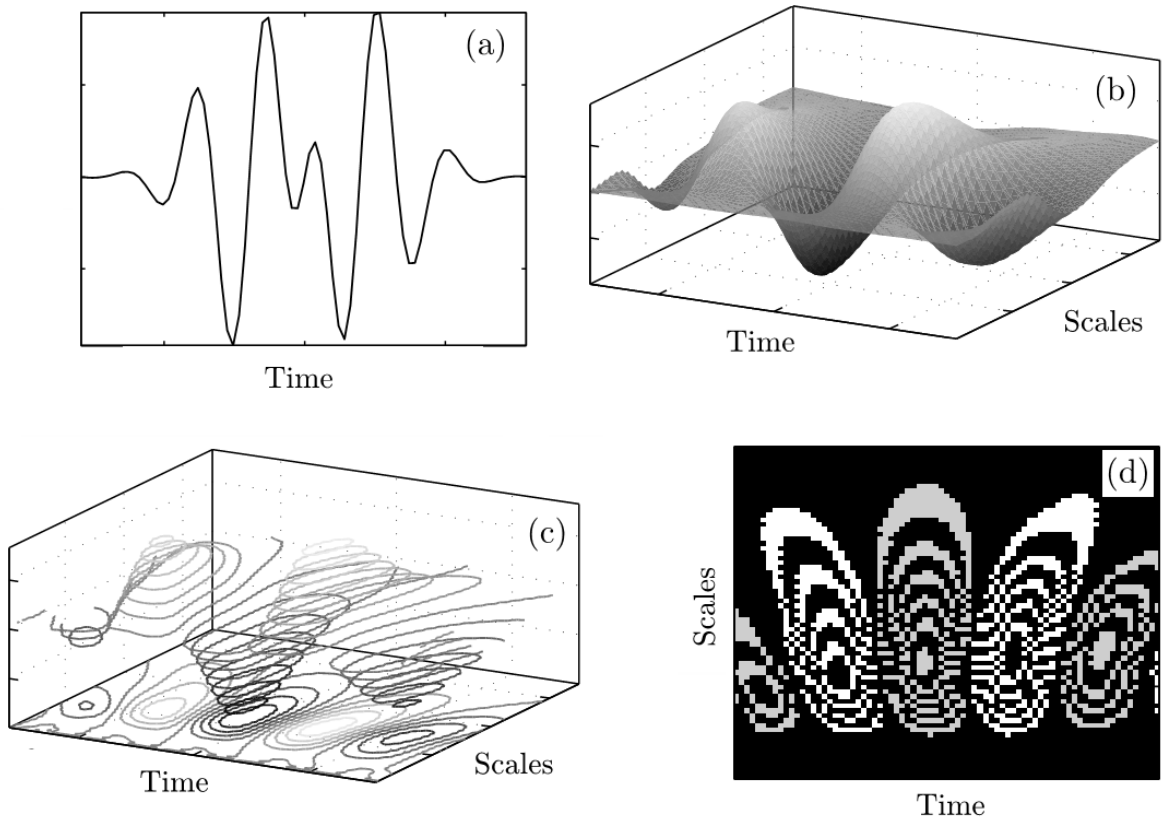

Figure 2: The dynamic wavelet fingerprint process (DWFP) uses a continuous wavelet transform to map a one-dimensional signal (a) to a three-dimensional surface of wavelet coefficients (b). Slicing this surface (c) and projecting the slices to a plane creates a two-dimensional time-scale image that often resembles a set of individual fingerprints (d). (Image modified and used by permission from [22])

The user has control of a large number of parameters in the DWFP creation and feature extraction process, which greatly affect the appearance of the fingerprint images, and thus the extracted features. There is no way to tell *a priori* which combination of parameters will create the ideal representation for a particular application. Past experience with analysis of DWFP images helps us to avoid an entirely brute force implementation for many applications. However, in some cases the signals to be analyzed are so noisy that humans are incapable of picking out useful patterns in the fingerprint images. For these applications we use the formal language of statistical pattern recognition and a computing cluster to run this feature extraction process in parallel for a large number of parameter combinations.

3 An application of the DWFP: Ultrasonic detection of flaws in microelectronics

In order to better illustrate the DWFP, we discuss an application using high-frequency pulse-echo ultrasound to detect subsurface flaws in microelectronic components [26]. Counterfeit, recycled, and maliciously modified integrated circuits have increasingly become a threat to the United States' information technology infrastructure, with estimated annual costs of $100 - $200 billion representing nearly 10% of all electronic equipment sold worldwide [27]. Suspected counterfeit router components need to be inspected quickly and nondestructively with portable equipment that doesn't require extensive training to operate. Although ultrasound in the 100 MHz frequency range routinely images the relevant subsurface features in microelectronic components, scanning acoustic microscopes are neither portable nor inexpensive, and they require the component to be submerged in

Table 1: A number of features are extracted from both the raw signal and the wavelet fingerprint image using the Matlab image processing toolbox *regionprops* analysis to create an optimized feature vector for each instance

Feature	**Description**
	Signal features
Raw signal	Original signal
Filtered signal	Wavelet filtered original signal
Raw PSD	Power Spectral Density of raw signal
Filtered PSD	Power Spectral Density of filtered signal
	Fingerprint image features
Area	Number of pixels in the region
Filled Area	Number of pixels in the bounding box (smallest rectangle that completely encloses the region)
Extent	Ratio of pixels in the region to pixels in bounding box, calculated as $\frac{\text{Area}}{\text{Area of bounding box}}$
Convex Area	Area of the convex hull (the smallest convex polygon that contains the area)
Equivalent Diameter	Diameter of a circle with the same area as the region, calculated as $\sqrt{\frac{4 \cdot \text{Area}}{\pi}}$
Solidity	Proportion of pixels in the convex hull to those also in the region, calculated as $\frac{\text{Area}}{\text{Convex Area}}$
xCentroid	Center of mass of the region along the horizontal axis
yCentroid	Center of mass of the region along the vertical axis
Major Axis Length	Pixel length of the major axis of the ellipse that has the same normalized second central moments as the region
Minor Axis Length	Pixel length of the minor axis of the ellipse that has the same normalized second central moments as the region
Eccentricity	Eccentricity of the ellipse that has the same normalized second central moments as the region, computed as the ratio of the distance between the foci of the ellipse and its major axis length
Orientation	Angle (in degrees) between the x-axis and the major axis of the ellipse that has the same second-moments as the region
Euler Number	Number of objects in the region minus the number of holes in those objects, calculated using 8-connectivity
Ridge count	Number of ridges in the fingerprint image, calculated by looking at the number of transitions between pixels on and off at each point in time

a bath of coupling water. Our alternative approach uses a custom-designed ultrasonic probe to directly contact the component surface without requiring submersion in water (Figure 3).

Data was collected from 19 flawed and 6 unflawed components, of two different physical package styles. For each component, ultrasound waveforms were acquired at approximately 30-48 locations in a rough grid pattern across the face of the component. In this way we can exploit positional information to better understand features that may be present in different regions of the component without the hassle of an automated high-precision scanner that would be necessary to create an image. To prevent operator bias, multiple measurements of each chip were taken. In total, 1710 different waveforms were collected, at frequencies of 100, 75, and 50 MHz.

By their nature, waveforms recorded from contact ultrasound measurements are much noisier than those

Figure 3: A benchtop apparatus consisting of an ultrasound pulser/receiver, high-speed digitizer, and transducer assembly mounted to a stabilizer arm is used to collect data from a flawed test component. The custom Matlab GUI displays the A-scan waveform during capture to allow the operator to ensure the system is working properly.

recorded in submerged ultrasound measurements. Careful design of the delay line can help separate those reflections we are most concerned about, but also creates more noise and false peaks from internal reflections. Finding the reflections we care about in these measurements by looking at the time-domain waveform is difficult, even for simple, homogeneous structures. For such complicated structures as microelectronics, and at such high frequencies where attenuation plays as important role, it is near impossible. As shown in Figure 4, even the spectrogram (STFT) doesn't provide any useful visual information.

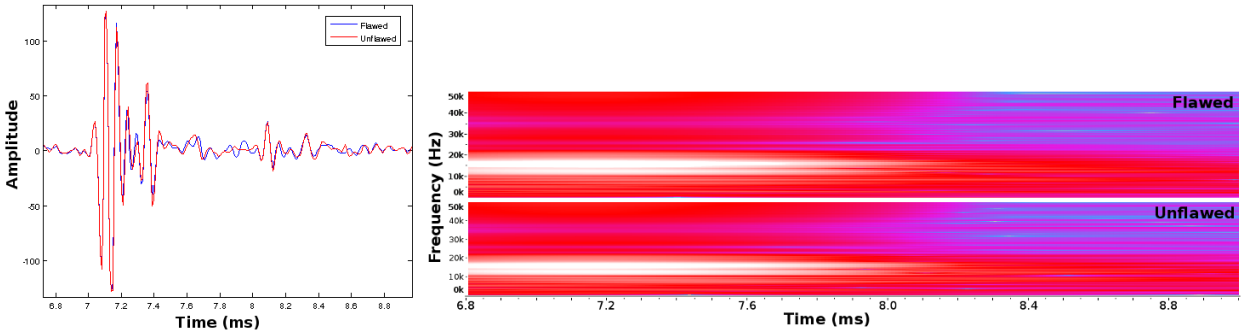

Figure 4: Neither the raw A-scan waveform (left) or the spectrogram image (right) show a noticeable difference between a flawed and unflawed sample at 50 MHz.

In order to analyze these waveforms and find features that correspond to internal structures of the components, we will use the time-frequency based DWFP analysis described above. Systematic investigation of the high-frequency (100 and 75 MHz) data was unable to identify obvious patterns useful to distinguish flawed and unflawed components. This is due to the location of the flaw underneath the silicon and the high level of attenuation in the plastic composite material. Analysis of the 50 MHz data showed clear features indicating the component's silicon layer, as well as features indicating delaminations distal to the silicon. Figure 5 shows three typical 50 MHz fingerprints from unflawed and flawed components, with a white feature that is absent when a

delamination is present.

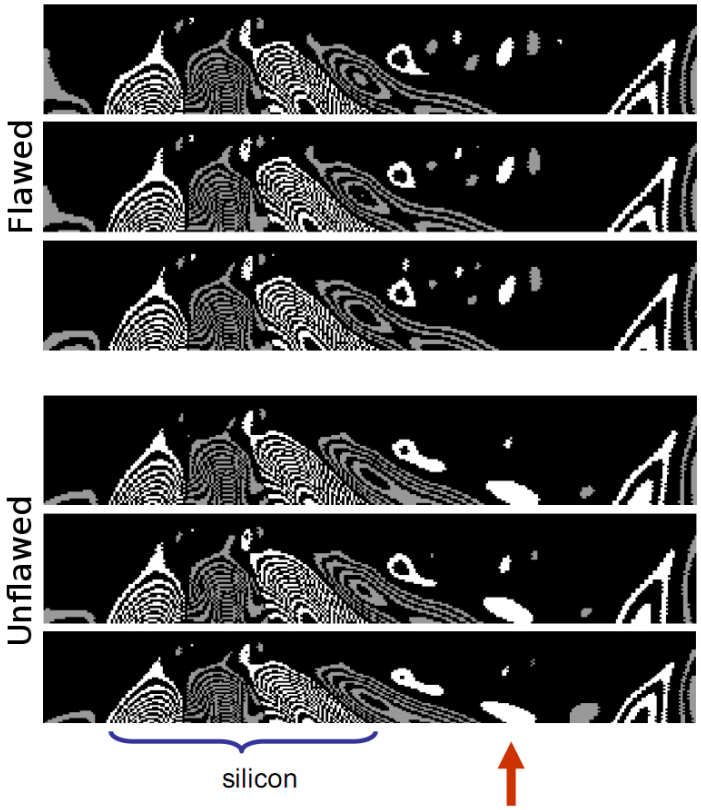

Figure 5: Comparison of the fingerprint images for three flawed (top) and three unflawed (bottom) components acquired at 50 MHz highlight differences in the signals not visible in the raw waveform. Since the horizontal axis is time delay of echoes (proportional to depth), we can identify the large feature with many ridges as the silicon layer and look for features that indicate a delamination immediately distal to this layer (red arrow). Here, the absence a stable white left-inclined oval indicates a delamination.

Now that a feature which indicates a delamination has been discovered, automated image processing routines can quickly look for this feature in each of the 30-48 measurement locations on a single component, making a binary flaw/no flaw decision at each point. Arranging these binary decisions according to the rough position where the measurements were acquired helps prevent false-positives. Contiguous regions of a positive flaw decision indicate a flawed component, which was verified with submerged C-scan ultrasound images (Figure 6).

For this moderately-sized proof-of-concept dataset, a human visual inspection of the fingerprint images highlighted features that were able to describe a microelectronic component as ‘flawed’ or ‘unflawed’. For more complicated multiclass detection and classification problems which require more than just a binary ‘good/bad’ decision, the main limitation of the DWFP analysis is the ability of humans to find stable, useful features in the massive datasets necessary to create a robust classifier. Here, feature selection algorithms such as Linear Discriminant Analysis (LDA) and Principal Component Analysis (PCA) running on computational clusters can be leveraged to create small, information-dense feature vectors which best describe the underlying signal.

This extended approach was applied to acoustic echolocation data, for which the goal was to classify vehicle types at distances exceeding 50 m based only on a reflected acoustic signals, and the massive amount of data required to form a robust data set (more than 4300 individual waveforms) makes human analysis of the fingerprint images impractical. Data was collected over a long period of time in noisy, unstructured environments, and large variation between signals means that aligning multiple signals and determining which part of the signal contains useful information is not a trivial task. Once trained, our DWFP-based approach was able to classify a previously-unseen echolocation waveform into one of five classes with with an accuracy of 94% [8].

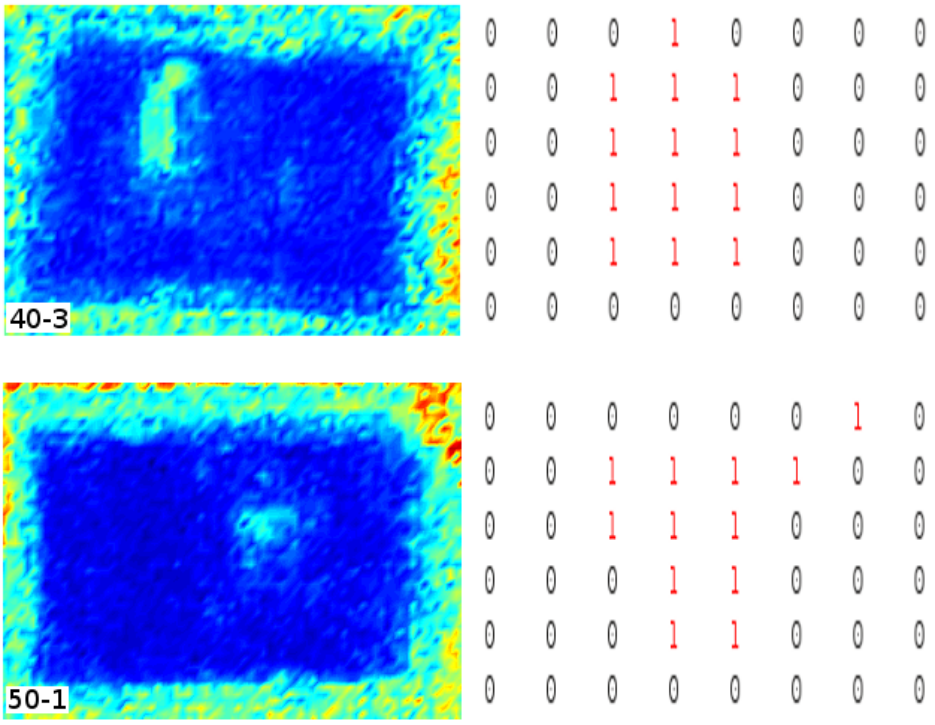

Figure 6: An image processing routine looks for the particular feature indicating a delamination in each of the 48 measurement locations on a single component. Contiguous regions of a flaw decision (right) indicate a flawed component, confirmed with submerged C-scan measurements (left).

References

[1] J. Hou and M. Hinders, "Dynamic wavelet fingerprint identification of ultrasound signals," *Mat. Eval.*, vol. 60, no. 9, pp. 1089–1093, 2002.

[2] M. Hinders, J. Hou, and J. M. Keon, "Wavelet processing of high frequency ultrasound echoes from multilayers," *Rev. of Progress in Quantitative Nondestructive Eval.*, vol. 24, pp. 1137–1144, 2005.

[3] C. A. Miller and M. K. Hinders, "Classification of flaw severity using pattern recognition for guided wave-based structural health monitoring," *Ultrasonics*, vol. 54, pp. 247–258, January 2014.

[4] J. Hou, M. Hinders, and S. Rose, "Ultrasonic periodontal probing based on the dynamic wavelet fingerprint," *J. Applied Signal Processing*, vol. 7, pp. 1137–1146, 2005.

[5] C. Bertoncini and M. Hinders, "Ultrasonic periodontal probing depth determination via pattern classification," in *31st Review of Progress in Quantitative Nondestructive Evaluation* (D. Thompson and D. Chimenti, eds.), vol. 29, pp. 1556–1573, AIP Press, 2010.

[6] M. Hinders, R. Jones, and K. R. Leonard, "Wavelet thumbprint analysis of time domain reflectometry signals for wiring flaw detection," *Eng. Intelligent Sys.*, vol. 15, no. 4, pp. 65–79, 2007.

[7] C. Bertoncini and M. Hinders, "Fuzzy classification of roof fall predictors in microseismic monitoring," *Measurement*, vol. 43, pp. 1690–1701, December 2010.

[8] E. Dieckman, *Use of pattern classification algorithms to interpret passive and active data streams from a walking-speed robotic sensor platform*. Doctoral dissertation, The College of William and Mary, May 2014.

[9] J. B. Allen and L. R. Rabiner, "A unified approach to short-time Fourier analysis and synthesis," *Proceedings of the IEEE*, vol. 65, no. 11, pp. 1558–1564, 1977.

[10] R. Crochiere, "A weighted overlap-add method of short-time Fourier analysis/synthesis," *IEEE Transactions on Acoustics, Speech and Signal Processing*, vol. 28, no. 1, pp. 99–102, 1980.

[11] L. Cohen, *Time-Frequency Analysis*. New Jersey: Prentice Hall, 1995.

[12] B. Boashash, "Note on the use of the Wigner distribution for time-frequency signal analysis," *IEEE Trans. on Acoustics, Speech, and Signal Processing*, vol. 36, pp. 1518–1521, Sep 1998.

[13] S. G. Mallat, "Relations between Gabor transforms and fractional Fourier transforms and their applications for signal processing," *IEEE Trans. on Signal Processing*, vol. 55, pp. 4839–4850, Oct 2007.

[14] S. G. Mallat, "A theory for multiresolution signal decomposition: The wavelet representation," *IEEE Trans. on Patt. Anal. and Machine Intell.*, vol. 11, no. 7, pp. 674–693, 1989.

[15] I. Daubechies, *Ten Lectures on Wavelets*. Philadelphia: CBMS-NSF Regional Conference Series in Applied Mathematics, 1992.

[16] D. J. Simons and C. F. Chabris, "Gorillas in our midst: Sustained inattentional blindness for dynamic events," *Perception*, vol. 28, no. 9, pp. 1059–1074, 1999.

[17] N. R. Pal and S. K. Pal, "A review on image segmentation techniques," *Pattern recognition*, vol. 26, no. 9, pp. 1277–1294, 1993.

[18] Y. J. Zhang, "A survey on evaluation methods for image segmentation," *Pattern recognition*, vol. 29, no. 8, pp. 1335–1346, 1996.

[19] Y. J. Zhang, "A review of recent evaluation methods for image segmentation," in *Sixth International Symposium on Signal Processing and its Applications*, vol. 1, pp. 148–151, IEEE, 2001.

[20] A. Abbate, J. Koay, J. Frankel, S. C. Schroeder, and P. Das, "Signal detection and noise suppression using a wavelet transform signal processor: application to ultrasonic flaw detection," *IEEE Transactions on Ultrasonics, Ferroelectrics, and Frequency Control*, vol. 44, no. 1, pp. 14–26, 1997.

[21] R. R. Coifman and D. L. Donoho, *Translation invariant de- noising*, vol. 103 of *Lecture Notes in Statistics*, pp. 125–150. New York, NY, USA: Springer-Verlag, 1995.

[22] C. A. Miller, *Intelligent feature selection techniques for pattern classification of time-domain signals*. Doctoral dissertation, The College of William and Mary, 2013.

[23] The MathWorks, Inc., *Matlab Image Processing Toolbox User Guide*, 2013.

[24] K. Karu and A. K. Jain, "Fingerprint classification," *Pattern recognition*, vol. 29, no. 3, pp. 389–404, 1996.

[25] J. Dai, J. Feng, and J. Zhou, "Robust and efficient ridge-based palmprint matching," *IEEE Transactions on Pattern Analysis and Machine Intelligence*, vol. 34, no. 8, pp. 1618–1632, 2012.

[26] E. A. Dieckman, M. Hinders, and J. Stevens, "Handheld high-frequency ultrasound for subsurface characterization of microelectronics," final technical report, Department of Applied Science, The College of William and Mary, December 2009. 67 pages.

[27] R. Spiegel, "Counterfeit components find new markets." `http://www.edn.com/article/CA6648803.html?text=counterfeit`, April 2009.